T. Magn. Soc. Jpn. (Special Issues)., **8**, 1-5 (2024) <Paper>

FeCo-based FeCoBPSiCr Amorphous Alloy and Powder with High Saturation Magnetic Flux Density and Corrosion Resistance

Y. Kajiura, A. Hasegawa, M. Hosono, K. Yoshidome, S. Otsuka*, H. Ohkubo* and H. Matsumoto
Materials Research Center, TDK Corporation, *656-1 Minamihadori, Narita-shi, Chiba 286-0805, Japan*
*Magnetics Business Group, TDK Corporation, *1-14-38 Takarada, Tsuruoka-shi, Yamagata 997-0011, Japan*

Soft magnetic materials are required to obtain high saturation magnetic flux density (B_s) and corrosion resistance for suppressing the magnetic saturation and supporting usage environments in power supplies of information and communication technology (ICT) devices with large current driving. This study investigated the magnetic characteristics, amorphous stability, and corrosion behavior of $(Fe_{0.7}Co_{0.3})_{88-x-y}B_{11}P_xSi_yCr_1$ and conventional $Fe_{79}Si_6B_{13}C_2$ amorphous alloys. A metallic ribbon comprising $(Fe_{0.7}Co_{0.3})_{82}B_{11}P_4Si_2Cr_1$ exhibited high B_s of 1.71 T and amorphous forming ability of 87 μm, sufficient to obtain a single amorphous phase even in powder morphology. The $(Fe_{0.7}Co_{0.3})_{82}B_{11}P_4Si_2Cr_1$ amorphous alloy ribbon with a high corrosion potential of −520 mV showed better corrosion resistance than conventional $Fe_{79}Si_6B_{13}C_2$ amorphous alloy with a low corrosion potential of −677 mV in water immersion tests. The $(Fe_{0.7}Co_{0.3})_{82}B_{11}P_4Si_2Cr_1$ amorphous alloy powder comprised a single amorphous phase and exhibited high B_s of 1.61 T, the same as that of the conventional $Fe_{79}Si_6B_{13}C_2$ amorphous alloy powder. Furthermore, an inductor using the $(Fe_{0.7}Co_{0.3})_{82}B_{11}P_4Si_2Cr_1$ amorphous alloy powder exhibited high DC-bias characteristics and excellent corrosion resistance compared to that using the conventional $Fe_{79}Si_6B_{13}C_2$ amorphous alloy powder. The results suggested that inductor using the $(Fe_{0.7}Co_{0.3})_{82}B_{11}P_4Si_2Cr_1$ amorphous alloy powder with high DC-bias characteristic and excellent corrosion resistance contribute to correspond to large current and high reliability of ICT devices.

Key words: soft magnetic materials, amorphous alloys, powders, corrosion resistance, inductors

1. Introduction

Recently, the demand for the Internet of Things (IoT) devices has increased significantly owing to the need for miniaturization of electronic devices with high performance and power density. In particular, inductors must exhibit excellent DC-bias characteristics corresponding to high-wattage ICs with large currents for high-power-density driving. Therefore, instead of ferrite materials with saturation magnetic flux density (B_s) < 0.5 T, inductors composed of metallic soft magnetic materials with B_s > 1.0 T, such as Fe-based amorphous and nanocrystalline alloys, are widely used to suppress magnetic saturation by a large current [1)-5)]. Currently, Fe-based soft magnetic materials are used as magnetic core materials for inductors. Moreover, achieving a high B_s is necessary to obtain high DC-bias characteristics. By contrast, inductor materials must possess high corrosion resistance to operate under usage environments. Moreover, from the perspective of sustainable development goals (SDGs), materials with high corrosion resistance are becoming increasingly important because they can be used for longer periods than those with low corrosion resistance. However, the corrosion resistance of a high B_s type Fe-based soft magnetic material is reduced by including a high Fe content due to achieving a high B_s [6)-7)]. The corrosion resistance of Fe-based soft magnetic materials with crystal grains, such as Fe-Si and Fe-based nanocrystalline alloys, is decreased because corrosion preferentially progresses from the grain boundaries [8)-9)]. Therefore, we focused on Fe-based amorphous alloys without crystal grains and reported a novel Fe-based $(Fe_{70}Co_{30})$BPSiCr alloy with high B_s and corrosion resistance [10)].

Corresponding author: Y. Kajiura
(e-mail: yoshiki.kajiura@tdk.com).

2. Experimental procedure

Master alloy ingots with FeCoBPSiCr and FeSiBC were prepared by induction melting using commercial raw materials such as Fe (99.9 mass %), Co (99.8 mass %), B (99.5 mass %), Si (99.999 mass %), Cr (99.9 mass %), and pre-alloyed FeP (99.9 mass %) in Ar. A single-roller melt-spinning method in Ar atmosphere was used to produce rapidly solidified ribbons with a width of 1 mm and thickness ranging from 60 μm to 105 μm. The structures of the as-quenched ribbons were identified by X-ray diffractometry (XRD) and transmission electron microscopy (TEM). The amorphous forming ability was determined from the thickness of the as-quenched ribbon with a single amorphous phase. To this end, as-quenched ribbons of varying thicknesses were fabricated. The maximum ribbon thickness without crystallization was determined to be the critical thickness. In particular, the degree of amorphous forming ability was indicated by the maximum as-quenched ribbon thickness without

crystallization, and a thickness of more than 60 μm was decided as a minimum critical thickness for powder production. The densities of the ribbons were measured using the Archimedean method with kerosene as the solvent. The B_s was measured using a vibrating sample magnetometer (VSM) under a maximum applied field of 1600 kA/m. Coercivity (H_c) was measured using an automatic coercive force meter (K-HC1000, Tohoku Steel Co.) under a maximum applied field of ~160 kA/m. The corrosion resistance was investigated using the corrosion potential (E_{corr}) and corrosion current density (i_{corr}) measured by linear sweep voltammetry (LSV) using a potentio-galvanostat. In a 0.5-M NaCl aqueous solution, the sweep speed for a spontaneous potential was 0.833 mV/s from −300 mV to +300 mV using both Ag/AgCl reference and Pt counter electrodes. After a 4-h immersion test in pure water, the appearance of a 20-μm-thick metallic ribbon was observed with an optical microscope. FeCoBPSiCr and FeSiBC powders were fabricated via gas atomization using high-pressure water. The average diameter of the powder was measured using a laser diffraction particle analyzer (HELOS). The densities of the powders were measured using a He gas pycnometer with a He purity of 5 N. The particle morphology of the powders was observed by scanning electron microscopy (SEM). Particle circularity (C) was determined as follows:

$$C = 2\sqrt{\pi A}/P \qquad (1)$$

where A is the particle area, and P is the perimeter determined using particle imaging (Morphologi-G3, Malvern Instruments). The thermal kinetic behavior was measured using differential scanning calorimetry (DSC) at a heating rate of 0.67 K/s. Inductor with the size of 2.0 (L) mm × 1.2 (W) mm × 0.8 (H) mm were prepared using the FeCoBPSiCr and FeSiBC powders. The products were plated with Ni after fabrication using the pressure-forming method with a Cu coil and resin-dispersed FeCoBPSiCr or FeSiBC particles. The permeability (μ_i) of the ring core with dimensions of 11 mm in outer diameter, 6.5 mm in inner diameter, and 2.5 mm in height at 1 MHz was measured by an impedance analyzer under a field of 0.13 A/m, and core loss (P_{cv}) was measured by a BH analyzer with 10 mT at 2 MHz. The DC bias characteristics of the inductance (L) were measured using an LCR meter at a maximum applied current of 9 A. The products were observed under an optical microscope.

3. Results

3.1 Dependence of alloy characteristics on the composition of $(Fe_{0.7}Co_{0.3})_{88-x-y}B_{11}P_xSi_yCr_1$

The dependence of amorphous forming ability and B_s on the compositions of $(Fe_{0.7}Co_{0.3})_{88-x-y}B_{11}P_xSi_yCr_1$ alloys were investigated. Fig. 1 (a) shows the dependence of amorphous forming ability on the compositions of $(Fe_{0.7}Co_{0.3})_{88-x-y}B_{11}P_xSi_yCr_1$ alloys. These alloys exhibited high amorphous forming ability ranging from 61 μm to 105 μm in the wide composition range. In particular, a high amorphous forming ability above 80 μm was observed for P contents of (3.5 to 4.5) at. % and Si contents of (1.5 to 2.0) at. %. Fig. 1 (b) shows the dependence of B_s on the compositions of the $(Fe_{0.7}Co_{0.3})_{88-x-y}B_{11}P_xSi_yCr_1$ alloys. A high B_s of more than 1.7 T was observed at high FeCo contents of more than 82 at. %, Si contents of (1 to 3) at. % and P contents of (3 to 4) at. %. From the above results, it is considered that composition optimizations for P, Si, and FeCo in the alloy are essential to achieve a high B_s and amorphous forming ability. Therefore, these results suggest that the $(Fe_{0.7}Co_{0.3})_{82}B_{11}P_4Si_2Cr_1$ alloy has the optimum composition because it exhibits a high amorphous forming ability of 87 μm with a B_s >1.7 T.

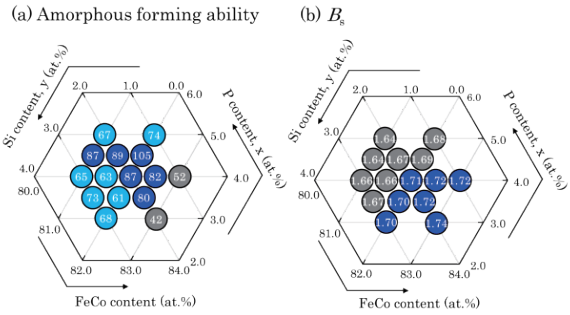

Fig. 1 Dependence of (a) amorphous forming ability and (b) B_s on the compositions of the $(Fe_{0.7}Co_{0.3})_{88-x-y}B_{11}P_xSi_yCr_1$ alloys.

The magnetic characteristics, corrosion potential, and corrosion current density of the $(Fe_{0.7}Co_{0.3})_{82}B_{11}P_4Si_2Cr_1$ alloy and the high-B_s-type conventional $Fe_{79}Si_6B_{13}C_2$ amorphous alloy with images of the metallic ribbon that appeared after the immersion tests are listed in Table 1.

The $(Fe_{0.7}Co_{0.3})_{82}B_{11}P_4Si_2Cr_1$ amorphous alloy showed the favorable magnetic characteristics compared to the conventional $Fe_{79}Si_6B_{13}C_2$ amorphous alloy and a higher amorphous forming ability than the conventional alloy. In addition, the $(Fe_{0.7}Co_{0.3})_{82}B_{11}P_4Si_2Cr_1$ amorphous alloy exhibited higher corrosion resistance than the conventional $Fe_{79}Si_6B_{13}C_2$ amorphous alloy in the appearance of the metallic ribbon after the immersion tests. In contrast, although the ribbon appearance of the $(Fe_{0.7}Co_{0.3})_{82}B_{11}P_4Si_2Cr_1$ amorphous alloy clearly showed

Table 1 Magnetic characteristics of B_s and H_c, corrosion characteristics of E_{corr} and i_{corr}, density of ribbons and optical microscope images of metallic ribbons in the $(Fe_{0.7}Co_{0.3})_{82}B_{11}P_4Si_2Cr_1$ and conventional $Fe_{79}Si_6B_{13}C_2$ amorphous alloys after 4-h immersion tests in pure water.

Composition	B_s (T)	H_c (A/m)	E_{corr} (mV)	i_{corr} (μA/cm²)	Amorphous forming ability (μm)	Density (g/cm³)	Ribbon appearance after immersion test
$(Fe_{0.7}Co_{0.3})_{82}B_{11}P_4Si_2Cr_1$	1.71	20.4	−520	23.7	87	7.69	
$Fe_{79}Si_6B_{13}C_2$	1.69	25.7	−677	53.1	60	7.38	

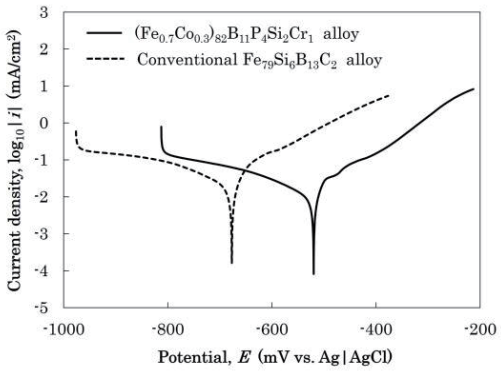

Fig. 2 Anodic polarization curves in 0.5 M NaCl aqueous solution at 0.833 mV/s sweep rate of the $(Fe_{0.7}Co_{0.3})_{82}B_{11}P_4Si_2Cr_1$ and the conventional $Fe_{79}Si_6B_{13}C_2$ alloy metallic ribbons.

a metallic color on the surface, the conventional $Fe_{79}Si_6B_{13}C_2$ amorphous alloy showed significant red rust on the surface. Fig. 2 shows the anodic polarization curves in 0.5-M NaCl aqueous solution at 0.833 mV/s sweep rate of the $(Fe_{0.7}Co_{0.3})_{82}B_{11}P_4Si_2Cr_1$ and conventional $Fe_{79}Si_6B_{13}C_2$ alloy metallic ribbons. High E_{corr} of −520 mV and low i_{corr} of 23.7 μA/cm² of the $(Fe_{0.7}Co_{0.3})_{82}B_{11}P_4Si_2Cr_1$ amorphous alloy led to the excellent corrosion resistance compared to the conventional $Fe_{79}Si_6B_{13}C_2$ amorphous alloy. Therefore, from the above results, the $(Fe_{0.7}Co_{0.3})_{82}B_{11}P_4Si_2Cr_1$ amorphous alloy showed higher B_s and corrosion resistance than the conventional $Fe_{79}Si_6B_{13}C_2$ amorphous alloy.

3.2 Powdarization of $(Fe_{0.7}Co_{0.3})_{82}B_{11}P_4Si_2Cr_1$ amorphous alloy

The morphology of the $(Fe_{0.7}Co_{0.3})_{82}B_{11}P_4Si_2Cr_1$ amorphous alloy powder was investigated. Fig. 3 shows the SEM images of the $(Fe_{0.7}Co_{0.3})_{82}B_{11}P_4Si_2Cr_1$ amorphous alloy powder, whereas Fig. 4 shows the particle circularities of $(Fe_{0.7}Co_{0.3})_{82}B_{11}P_4Si_2Cr_1$ and the conventional $Fe_{79}Si_6B_{13}C_2$ alloy powders. The $(Fe_{0.7}Co_{0.3})_{82}B_{11}P_4Si_2Cr_1$ amorphous alloy powder consisted of spherical particles with smooth surfaces (Fig. 3). In addition, the $(Fe_{0.7}Co_{0.3})_{82}B_{11}P_4Si_2Cr_1$ amorphous alloy powder showed a high circularity of 0.981 compared to the conventional $Fe_{79}Si_6B_{13}C_2$ alloy powder with a low

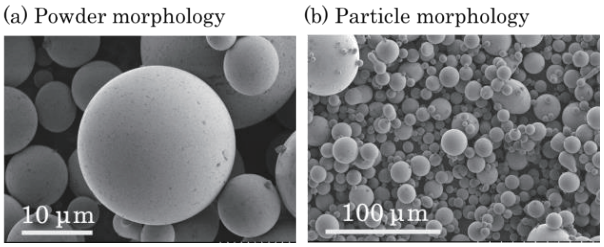

Fig. 3 SEM images of the (a) powder and (b) particle morphology in the $(Fe_{0.7}Co_{0.3})_{82}B_{11}P_4Si_2Cr_1$ amorphous alloy powder.

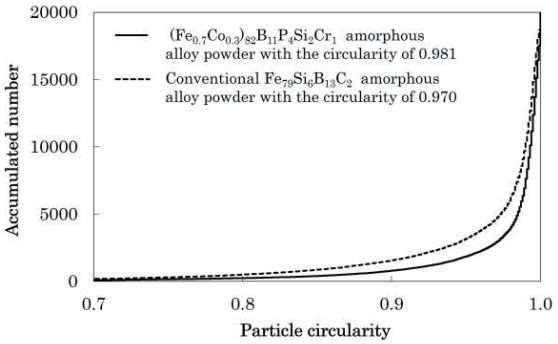

Fig. 4 Particle circularity of the $(Fe_{0.7}Co_{0.3})_{82}B_{11}P_4Si_2Cr_1$ and the conventional $Fe_{79}Si_6B_{13}C_2$ alloy powders.

circularity of 0.970, as shown in Fig. 4.

Fig. 5 shows the melting point (T_m) and liquid phase point (Tl) of $(Fe_{0.7}Co_{0.3})_{82}B_{11}P_4Si_2Cr_1$ and conventional $Fe_{79}Si_6B_{13}C_2$ alloy powders. Low T_m and Tl were observed for the $(Fe_{0.7}Co_{0.3})_{82}B_{11}P_4Si_2Cr_1$ amorphous alloy powder compared to those of the conventional $Fe_{79}Si_6B_{13}C_2$ amorphous alloy powder. The viscosity of the melting alloy strongly depends on the ΔT (= $T - T_m$, where T indicates the molten metal temperature during atomization), and the viscosity decreases by increasing ΔT. This suggests that the $(Fe_{0.7}C_{0.3})_{82}B_{11}P_4Si_2Cr_1$ amorphous alloy powder with the low T_m of 1270 K is low viscosity of molten metal during atomization compared to the conventional $Fe_{79}Si_6B_{13}C_2$ amorphous alloy powder with high T_m of 1360 K [11),12)]. Moreover, spherical particles are easily obtained in case the alloy with low viscosity in the gas-atomized process [13)]. Therefore, it is considered that particles with high circularity were obtained by the viscosity of the $(Fe_{0.7}Co_{0.3})_{82}B_{11}P_4Si_2Cr_1$ amorphous alloy molten metal during atomization, which was low due to the low T_m of the $(Fe_{0.7}Co_{0.3})_{82}B_{11}P_4Si_2Cr_1$ amorphous alloy.

Fig. 6 shows a TEM image of the $(Fe_{0.7}Co_{0.3})_{82}B_{11}P_4Si_2Cr_1$ amorphous alloy particles with the selected area electron diffraction (SAED) pattern. The $(Fe_{0.7}Co_{0.3})_{82}B_{11}P_4Si_2Cr_1$ amorphous alloy powder was composed of a single amorphous phase. The XRD

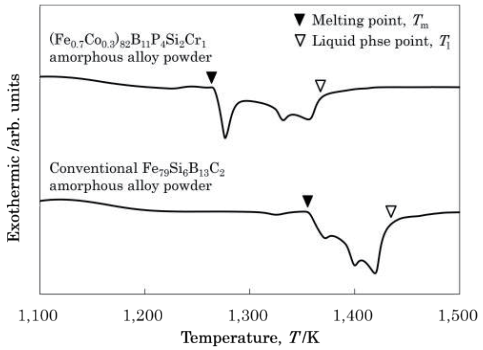

Fig. 5 DSC curves of the $(Fe_{0.7}Co_{0.3})_{82}B_{11}P_4Si_2Cr_1$ and the conventional $Fe_{79}Si_6B_{13}C_2$ alloy powders.

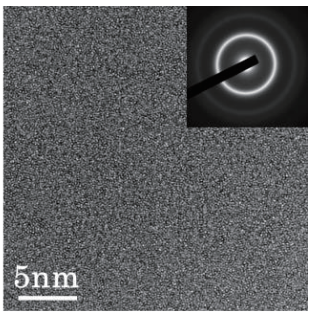

Fig. 6 TEM image of the $(Fe_{0.7}Co_{0.3})_{82}B_{11}P_4Si_2Cr_1$ amorphous alloy particle with SAED pattern.

patterns of the $(Fe_{0.7}Co_{0.3})_{82}B_{11}P_4Si_2Cr_1$ and conventional $Fe_{79}Si_6B_{13}C_2$ alloy powders are shown in Fig. 7. The $(Fe_{0.7}Co_{0.3})_{82}B_{11}P_4Si_2Cr_1$ amorphous alloy powder shows a halo pattern, indicating an amorphous structure with the same level of amorphous stability as that of the conventional $Fe_{79}Si_6B_{13}C_2$ alloy powder. Therefore, the $(Fe_{0.7}Co_{0.3})_{82}B_{11}P_4Si_2Cr_1$ amorphous alloy with an amorphous forming ability of more than 80 μm can be fabricated as the amorphous powder consists of a single amorphous phase.

3.3 Electro-magnetic characteristics of $(Fe_{0.7}Co_{0.3})_{82}B_{11}P_4Si_2Cr_1$ amorphous alloy powder

Table 2 lists the representative characteristics of the $(Fe_{0.7}Co_{0.3})_{82}B_{11}P_4Si_2Cr_1$ and conventional $Fe_{79}Si_6B_{13}C_2$ alloy powders. The $(Fe_{0.7}Co_{0.3})_{82}B_{11}P_4Si_2Cr_1$ amorphous alloy powder showed the same B_s level (1.61 T) as that of the conventional $Fe_{79}Si_6B_{13}C_2$ alloy powder. However, a slightly higher permeability was observed in the $(Fe_{0.7}Co_{0.3})_{82}B_{11}P_4Si_2Cr_1$ amorphous alloy powder because H_c of the $(Fe_{0.7}Co_{0.3})_{82}B_{11}P_4Si_2Cr_1$ amorphous alloy powder was lower than that of the conventional $Fe_{79}Si_6B_{13}C_2$ alloy powder. In addition, although B_s of the powders decreased compared with that of the metallic ribbons, it is considered that B_s decrease led to a decrease in the density of the powders. In gas atomization, hollow particles including air are observed especially in the powder, which is presumed the cause of the decrease in the density of the powders.

Table 2 Average diameter, density of powders, packing density, magnetic characteristics of B_s and H_c, electro-magnetic characteristics of μ_i, and P_{cv} in the $(Fe_{0.7}Co_{0.3})_{82}B_{11}P_4Si_2Cr_1$ and the conventional $Fe_{79}Si_6B_{13}C_2$ amorphous alloy powders.

Composition	Average diameter (μm)	Density (g/cm^3)	B_s (T)	H_c (A/m)	Packing density (%)	μ_i	P_{cv} (kW/m^3)
$(Fe_{0.7}Co_{0.3})_{82}B_{11}P_4Si_2Cr_1$	20.7	7.30	1.61	80	73.9	25.1	745
$Fe_{79}Si_6B_{13}C_2$	22.4	7.12	1.60	137	73.6	24.2	774

Fig. 8 shows the DC-bias characteristics of inductors with the dimensions of 2.0 (L) mm × 1.2 (W) mm × 0.8 (H) mm fabricated by using the $(Fe_{0.7}Co_{0.3})_{82}B_{11}P_4Si_2Cr_1$ and conventional $Fe_{79}Si_6B_{13}C_2$ amorphous alloy powders. Moreover, their appearances are shown in Fig. 9. The inductor fabricated using the $(Fe_{0.7}Co_{0.3})_{82}B_{11}P_4Si_2Cr_1$ amorphous alloy powder showed slightly better DC-bias characteristics than those fabricated using the conventional $Fe_{79}Si_6B_{13}C_2$ amorphous alloy powder. It is considered that the $(Fe_{0.7}Co_{0.3})_{82}B_{11}P_4Si_2Cr_1$ amorphous alloy powder exhibited a slightly high DC bias characteristic in the inductor consisting of the integrally molded structure with Cu coil and magnetic core because a packing condition of that was improved by the high circularity of the $(Fe_{0.7}Co_{0.3})_{82}B_{11}P_4Si_2Cr_1$ amorphous alloy powder. However, further investigation is required regarding the relationship between the particle circularity and DC-bias characteristics.

In addition, the inductor fabricated using the $(Fe_{0.7}Co_{0.3})_{82}B_{11}P_4Si_2Cr_1$ amorphous alloy powder exhibited excellent corrosion resistance compared with that fabricated using the conventional $Fe_{79}Si_6B_{13}C_2$ amorphous alloy powder.

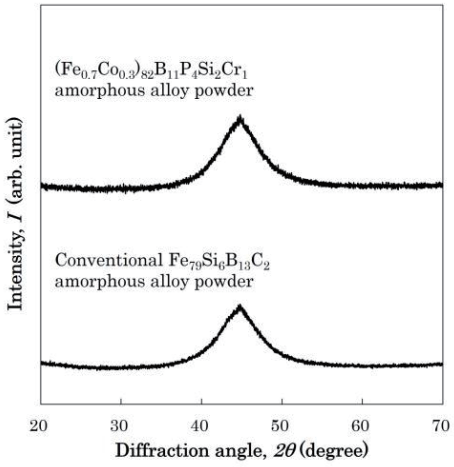

Fig. 7 XRD patterns of the $(Fe_{0.7}Co_{0.3})_{82}B_{11}P_4Si_2Cr_1$ and the conventional $Fe_{79}Si_6B_{13}C_2$ alloy powders.

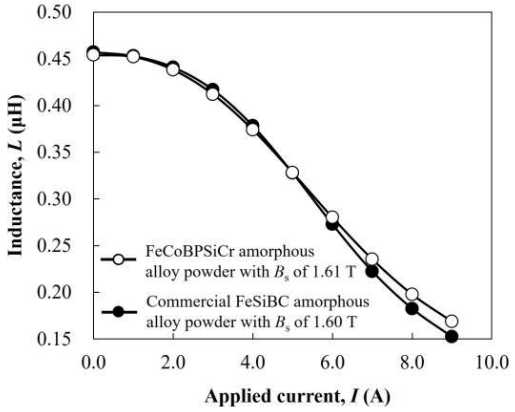

Fig. 8 DC-bias characteristics of the $(Fe_{0.7}Co_{0.3})_{82}B_{11}P_4Si_2Cr_1$ and the conventional $Fe_{79}Si_6B_{13}C_2$ amorphous alloy powders.

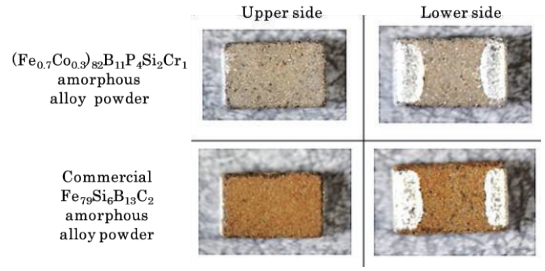

Fig. 9 Optical microscope images of products with the dimensions of 2.0 mm (L) × 1.2 (W) mm × 0.8 (H) mm using the $(Fe_{0.7}Co_{0.3})_{82}B_{11}P_4Si_2Cr_1$ and the conventional $Fe_{79}Si_6B_{13}C_2$ amorphous alloy powders.

Even after cutting and electrode plating, the inductor fabricated using the $(Fe_{0.7}Co_{0.3})_{82}B_{11}P_4Si_2Cr_1$ amorphous alloy powder exhibited a gray color with the same color as the powder itself. In contrast, red rust was clearly observed on the surface of the product fabricated using the conventional $Fe_{79}Si_6B_{13}C_2$ amorphous alloy powder. From the above results, the $(Fe_{0.7}Co_{0.3})_{82}B_{11}P_4Si_2Cr_1$ amorphous alloy with B_s of more than 1.7 T is recognized that the alloy shows a high B_s of 1.61 T and an excellent corrosion resistance in also the powder. Therefore, the inductor fabricated using $(Fe_{0.7}Co_{0.3})_{82}B_{11}P_4Si_2Cr_1$ amorphous alloy powder contribute to the miniaturization of electronic devices by exhibiting high DC-bias characteristics. Moreover, their excellent corrosion resistance contributes to maintaining a high reliability in various usage environments.

4. Conclusions

The magnetic characteristics, amorphous stability, and corrosion behavior of $(Fe_{0.7}Co_{0.3})_{88-x-y}B_{11}P_xSi_yCr_1$ amorphous alloys and powder were investigated in this study. The conclusions drawn from the results are as follows.

(1) $(Fe_{0.7}Co_{0.3})_{82}B_{11}P_4Si_2Cr_1$ amorphous alloy exhibited a high amorphous forming ability of 87 μm, which is required for powderization, and a high B_s of 1.71 T.

(2) With regard to the corrosion behavior, the $(Fe_{0.7}Co_{0.3})_{82}B_{11}P_4Si_2Cr_1$ amorphous alloy with a high E_{corr} value of −520 mV and a low i_{corr} value of 23.7 μA/cm² showed a higher corrosion resistance than commercial $Fe_{79}Si_6B_{13}C_2$ amorphous alloy without red rust on the metallic ribbon surface when immersed in pure water.

(3) The $(Fe_{0.7}Co_{0.3})_{82}B_{11}P_4Si_2Cr_1$ amorphous alloy powder consisted of a single amorphous phase, as observed from the TEM images and XRD and SAED patterns.

(4) An inductor using the $(Fe_{0.7}Co_{0.3})_{82}B_{11}P_4Si_2Cr_1$ amorphous alloy powder exhibited high DC-bias characteristics and excellent corrosion resistance compared to that using the commercial $Fe_{79}Si_6B_{13}C_2$ amorphous alloy powder.

References

1) F. Luborsky, J. Becker, J. Walter, H. Liebermann: *IEEE Trans. Magn*., **15**, 1146 (1979).
2) A. Kojima, S. Ito, A. Makino and A. Inoue: *Mater. Trans. JIM*, **42**, 1535 (2001).
3) Y. Yoshizawa, S. Oguma and K. Yamauchi: *Appl. Phys.*, **64**, 6044 (1988).
4) A. Urata, H. Matsumoto, S. Yoshida and A. Makino: *IEEE Trans. Magn.*, **47**, 3177 (2011).
5) H. Matsumoto, Y. Kajiura, M. Hosono, A. Hasegawa, H. Kumaoka, K. Yoshidome, S. Mori: *AIP Advances*, **12**, 035312 (2022).
6) D.D. Coimbrao, G. Zepon, G.Y. Koga, D.A. Godoy Perez, F.H. Paes de Almeida, V. Roche, J.-C. Lepretre, A.M. Jorge Jr., C.S. Kiminami, C. Bolfarini, A. Inoue, W.J. Botta: *J. Alloys Compd.*, **826**, 154123 (2020).
7) G. Palumbo, D. Dunikowski, R. Wirecka, T. Mazur, U. Lelek-Borkowska, K. Wawer, J. Banas: *Materials*, **14**, 5084 (2021).
8) Y. Han, F.L. Kong, F.F. Han, A. Inoue, S.L. Zhu, E. Shalaan, F. Al-Marzouki: *Intermetallics,* **76**, 18 (2016).
9) D.D. Xu, B.L. Zhou, Q.Q. Wang, J. Zhou, W.M. Yang, C.C. Yuan, L. Xue, X.D. Fan, L.Q. Ma, B.L. Shen: *Corros. Sci*., **138**, 20 (2018).
10) A. Hasegawa, Y. Kajiura, M. Hosono, K. Yoshidome, H. Matsumoto: *AIP Advances*, **13**, 025120 (2023).
11) M. Hirai: ISIJ International, **33**, 1182, (1993).
12) V. S. Tsepelev and Y. N. Starodubtsev: *Nanomaterials*, **11**, 108 (2021).
13) E. S. Barreto, M. Frey, J. Wegner, A. Jose, N. Neuber, R. Busch, S. Kleszczynski, L. Madler and V. Uhlenwinkel: *Materials & Design*, **215**, 110519 (2022).

Received Oct. 12, 2023; Accepted Dec. 9, 2023